Chapter 4

RADIO SPECTRAL DIAGNOSTICS

Dale E. Gary

Center for Solar-Terrestrial Research, New Jersey Institute of Technology, Newark, NJ 07102 USA

dgary@njit.edu

G. J. Hurford

Space Sciences Laboratory, University of California, Berkeley, CA 94720

ghurford@ssl.berkeley.edu

Abstract   We review solar radio emission from the perspective of imaging spectroscopy. Radio emission mechanisms differ in their spectral properties, which can be used to determine parameters of the emitting particles and the ambient solar atmosphere in the emitting volume. After generation, the propagation of radiation in the solar atmosphere leads to changes in the spectrum that can be exploited to gain further information about the atmospheric parameters along the line of sight.

1.   Introduction

Spectral diagnostics have a long history of importance in astrophysics. In fact, the "new science" of astrophysics was born from astronomy with the advent of spectroscopy in the mid-19th century. Solar radio physics was strongly influenced from the beginning by the spectral viewpoint, with the discovery and classification of burst types by Wild & McCready (1950; types I–III), Boischot (1959; type IV), and Wild *et al.* (1959; type V), based on their appearance on spectrographs. Multifrequency radiometers and radio spectrographs, which measure the spatially-integrated flux density from the Sun, have been and will continue to be important for solar diagnostics, but their use for quantitative work, especially for incoherent emission processes, is often frustrated by the inhomogeneity of the Sun and the inability to spatially associate sources with observations at other wavelengths. Radioheliographs (e.g. Nançay Radiohelio-

graph and Nobeyama Radioheliograph) and synthesis telescopes (e.g. Wester-bork Synthesis Radio Telescope and Very Large Array) can make high-quality images of the Sun, but operate at only a few widely-spaced frequencies. The only instrument that combines imaging with frequency resolution and coverage adequate for spectral diagnostics is the Owens Valley Solar Array (OVSA), but its small number of antennas and limited spatial resolution fall short of what is needed to fully exploit the diagnostic potential of radio imaging spectroscopy.

The Frequency Agile Solar Radiotelescope (FASR) is envisioned as the first solar radio instrument to combine the spectral and spatial capabilities needed to fully exploit this diagnostic potential. Many of the preceding chapters discuss the multiple-frequency imaging capabilities envisioned for FASR, but this chapter focuses on an alternative viewpoint which, while equivalent, can yield important new insights. Instead of considering the data-cube as a stack of independent images whose morphology changes with frequency, we view the data-cube vertically and consider each pixel in the images to have an associated spectrum.

Such a spectrum is referred to as a *brightness temperature spectrum*, since, for a spatially-resolved image, it is the spectrum of surface brightness, expressed in units of temperature. This is in contrast to the spatially-integrated spectrum. The two are related by the Rayleigh-Jeans approximation for the Planck function

$$S_\nu = \int \frac{2k_B T_b \nu^2}{c^2} d\Omega, \tag{4.1}$$

where S_ν is the flux density (W m^{-2} Hz^{-1}) at frequency, ν (Hz), from an element of solid angle, $d\Omega$, and k_B is the Boltzmann constant. The brightness temperature T_b is the "temperature equivalent brightness" of the emission, and is the essential quantity that contains all of the physics. For example, in the case of optically thick thermal emission it is just the electron temperature. For optically thick nonthermal emission it is an "effective" temperature related to the energy $k_B T_{\text{eff}}$ of the emitting electrons. As we will discuss in more detail shortly, a surprisingly large number of physical parameters can be deduced from a precisely measured brightness temperature spectrum.

In using the terms thermal and nonthermal, above, we restrict ourselves to incoherent emission, where each electron produces radiation independently of the others in the source. However, emission is possible from electrons that act coherently, in phase with the wave mode exciting the electron motion. The brightness of such coherent emission loses its diagnostic power for determining electron energies, but rather reflects the growth rate of the responsible waves, which may be Langmiur waves, electron-cyclotron waves or others. However, when the mechanism responsible for such coherent emission can be identified, the emitting frequency, polarization, and timescale for brightness changes can

provide diagnostics on the ambient density, magnetic field strength, speed of the disturbance, inherent size of the source, and perhaps other parameters.

2. Characteristic Frequencies of the Solar Atmosphere

To gain an overview of the power of radio spectral diagnostics, it is necessary to have an appreciation for radio emission processes in the Sun and solar wind over more than 6 decades in frequency, from < 30 kHz (typical plasma frequency at Earth) to > 30 GHz. FASR will cover approximately the upper half of these 6 decades of frequency. Although a bewildering variety of emission mechanisms vie for dominance over this wide spectral range, much of the apparent complexity exhibited by solar bursts can be understood in terms of three characteristic frequencies (Gary & Hurford 1988). The three relevant frequencies (Hz) are the plasma frequency,

$$\nu_p = 8.98 \times 10^3 \sqrt{n_e}, \tag{4.2}$$

the frequency at which free-free emission reaches optical depth unity

$$\nu(\tau_{\mathrm{ff}} = 1) \approx 0.5 n_e T_e^{-3/4} L^{1/2}, \tag{4.3}$$

and the electron gyrofrequency

$$\nu_B = 2.8 \times 10^6 B. \tag{4.4}$$

In equations (4.2–4.4), n_e is the electron density in cm^{-3}, T_e is the electron temperature in K, L is the relevant scale length in cm for free-free emission (the density scale height in the case of an isothermal corona), and B is the magnetic field strength in G.

Figure 4.1 relates these characteristic frequencies to height in the solar atmosphere for a nominal solar model, providing a heuristic indication for why emission mechanisms change with height. In general, the characteristic frequency that appears highest in the figure determines the emission mechanism. Broadly speaking, plasma emission dominates at frequencies from 30 kHz to several hundred MHz, covering heights greater than 0.2 $R_\odot$ above the photosphere. The dominance of plasma emission over this range is simply because the plasma level lies above the $\tau_{\mathrm{ff}} = 1$ level at these frequencies. At decimetric frequencies (200 MHz–1 GHz), the plasma level in active regions is generally below the $\tau_{\mathrm{ff}} = 1$ level, but plasma emission may still be important because of the inhomogeneity of the corona in this height range, and the extremely high brightness of the coherent plasma emission, which can reach an intrinsic brightness of 10^{15} K. Outside of bursts, the emission in this range is thermal or slightly nonthermal, but burst emission is still dominated by coherent plasma emission.
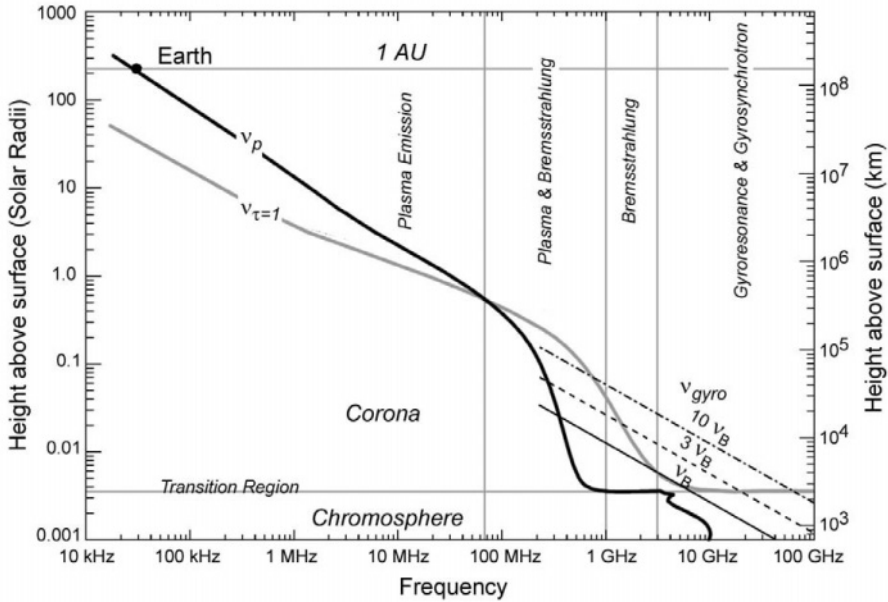
Figure 4.1. Characteristic radio frequencies for the solar atmosphere. The upper-most characteristic frequency at a given frequency determines the dominant emission mechanism. The plot is meant to be schematic only, and is based on a model of temperature, density, and magnetic field as follows: The density is based on the VAL model B (Vernazza *et al.* 1981), extended to 10^5 km by requiring hydrostatic equilibrium, and then matched by a scale factor to agree with 5 × the Saito *et al.* (1970) minimum corona model above that height (the factor of 5 was chosen to give 30 kHz as the 1 AU plasma frequency). Temperature was based on the VAL model to about 10^5 km, then extended to 2×10^6 K by a hydrostatic equilibrium model. The temperature is then taken to be constant to 1 AU. The magnetic field strength was taken to be the typical value for active regions given by Dulk & McLean (1978), $B = 0.5(R/R_\odot - 1)^{1.5}$. For the $\nu(\tau_{ff} = 1)$ curve, a scale height L is needed. We used $L = H_0(T/T_0)(R/R_\odot)^2$ where $H_0 = 0.1R_\odot$ and $T_0 = 2 \times 10^6$ K. Near the Sun, the curves apply to active regions.

Three lines are shown for gyroemission, representing the cyclotron frequency and its harmonics. The cyclotron line ($\nu = \nu_B$) is generally not relevant for the solar corona within active regions, but rather the emission occurs typically at the third harmonic $\nu = 3\nu_B$. Figure 4.1 shows that the $3\nu_B$ line lies above the $\tau_{ff} = 1$ level down to 1–2 GHz, and extends up in frequency to ~ 20 GHz—both of which agree well with the observed range. During bursts, gyroemission is more typically at $\nu = 10\nu_B$, from which we see that gyroemission during bursts can extend to 800–900 MHz in the decimetric range. At mm wavelengths ~ 100 GHz, bursts can be dominated by either free-free or gyroemission, depending on the number and energy of emitting particles. Outside of flares, the emission above 20 GHz is entirely due to free-free emission.

3.   Plasma Emission Diagnostics

As we mentioned above, the brightness temperature due to coherent mechanisms does not provide a diagnostic of the electron energy distribution, as incoherent mechanisms do. But as discussed in more detail in Chapter 10, other features of the spectrum are rich in diagnostics. A prime example is the frequency drift rate of type III bursts. These are due to beams of electrons traveling upward or downward in the solar corona, which generate emission at the plasma frequency or its second harmonic. Hence, the emission frequency depends only on the local electron density, according to equation 4.1. Given a model of density vs. height, the frequency drift rate can be converted to beam velocity, which is typically of order $0.1c$. Alternatively, imaging observations at many frequencies, such as FASR will give the trajectory of the beam and hence the run of electron density along the trajectory. When type III bursts with both positive and negative frequency drifts are seen (see Figure 2.7 of Chapter 2, and Figure 10.1 of Chapter 10), imaging observations should pinpoint the location of the acceleration site.

Type II bursts, also due to plasma emission, are excited by the passage of a shock wave. Similar to the case of type III bursts, the frequency drift rate, combined with spectral imaging, gives the ambient density and speed of the shock. Some type II bursts show "herring bone" structure due to excitation of electron beams from the shock front. Spectral imaging of such bursts should give rich diagnostics of particle acceleration at shocks by giving the local direction of the magnetic field along the shock (from the trajectories of the type IIIs) and the ambient density along the shock (from the frequency of emission).

As described in Chapter 10, many other types of coherent emission occur in the decimetric and metric wavelength ranges, for which spectral imaging may provide new plasma diagnostics. However, much more must be learned about the emission mechanisms before the full diagnostic potential can be realized. Quasi-periodic pulsations, for example, can potentially give magnetic field diagnostics if the oscillating magnetic loop geometry is known from imaging observations. FASR's combined spatial and spectral capabilities will yield new insights into the myriad coherent burst types, and perhaps give a better understanding of the emission mechanisms necessary for new diagnostics that are not yet possible.

4.   Free-Free Diagnostics

At radio wavelengths, free-free emission, or bremsstrahlung, is derived from consideration of collisions of electrons on ions in the small-angle approximation. An expression for free-free opacity from thermal electrons, relevant to

conditions of the solar atmosphere, was given by Dulk (1985) as

$$\kappa_\nu \approx \sum_i \frac{1}{3c} \left(\frac{2}{\pi}\right)^{1/2} \frac{\nu_p^2}{\nu^2} \frac{4\pi Z_i^2 n_i e^4}{m_e^{1/2}(k_B T)^{3/2}} \frac{\pi}{\sqrt{3}} G(T,\nu) \tag{4.5}$$

$$\approx 9.78 \times 10^{-3} \frac{n_e}{\nu^2 T^{3/2}} \sum_i Z_i^2 n_i \times \begin{cases} 18.2 + \ln T^{3/2} - \ln\nu & (T < 2 \times 10^5 K) \\ 24.5 + \ln T - \ln\nu & (T > 2 \times 10^5 K) \end{cases} \tag{4.6}$$

where ν_p is the plasma frequency (eq. 4.2), Z_i and n_i are the ion charge and number density, respectively ($\sum_i Z_i^2 n_i \approx 1.2 n_e$ for the solar corona), m_e is the electron mass, and G is the free-free "gaunt factor" related to the Coulomb logarithm. As discussed in Chapter 6, for free-free emission from the solar atmosphere the corona has an appreciable optical thickness at low frequencies, becoming optically thin at higher frequencies whereby the lower-lying chromosphere becomes visible. As frequency increases further, we see to slightly lower depths in the chromosphere, but it remains optically thick to the highest radio frequencies. Even at submillimeter wavelengths the chromosphere is optically thick well above the temperature minimum region (Bastian *et al.* 1993).

The equation of radiative transfer becomes

$$T_b = T_{\text{chr}} \exp^{-\tau_{cor}} + T_{\text{cor}}(1 - \exp^{-\tau_{cor}}) \tag{4.7}$$

where T_{chr} is the electron temperature of the chromosphere, T_{cor} is the electron temperature of the corona, and $\tau_{\text{cor}} = \int \kappa \, dl$ is the optical depth of the corona. Figure 4.2 shows the spectral shape that results from an isothermal corona at $T_{\text{cor}} = 10^6$ K overlying an isothermal chromosphere at $T_{\text{chr}} = 10^4$ K (solid line), and after subtracting the background chromosphere (dotted line).

Changing the temperature and density (or column emission measure $\int n^2 dl$) of the corona merely shifts the (dashed) spectrum in the directions indicated by the arrows in Figure 4.2, *without changing the spectral shape.* The lengths and directions of the arrows indicate the effect of quadrupling the relevant parameter labeling the arrows. Gary & Hurford (1988) called such spectra "Universal Spectra," to indicate that the shape is invariant to changes in plasma parameters. The Universal Spectra are strictly valid only for homogeneous sources, and variations along the line of sight can change the spectral shape. An example of the use of this spectral diagnostic to deduce coronal temperature and density as a function of position in an active region was given by Gary & Hurford (1994—See Fig. 2.2 of Chapter 2).

FASR will produce far higher quality brightness temperature spectra, at much better spatial resolution, than any previously available. As noted in Chapter 6, the polarization characteristics of such spectra provide a diagnostic of the longitudinal magnetic field strength. The more precise measurements from FASR will permit more realistic modeling of the line-of-sight variations of tempera-
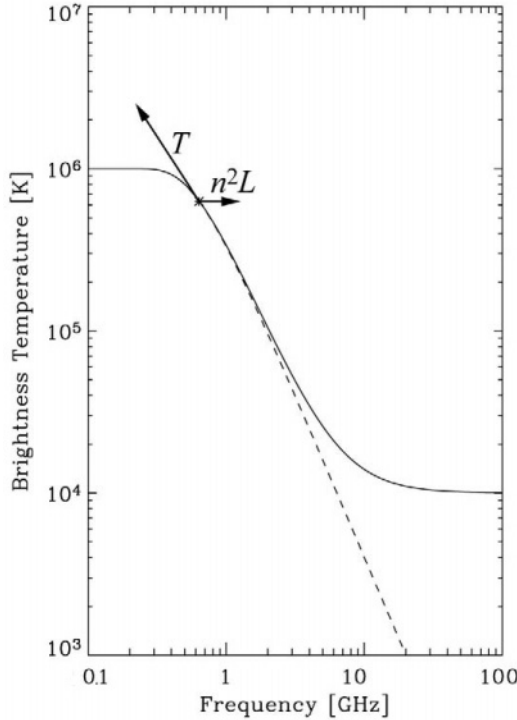
Figure 4.2. A "Universal Spectrum" for free-free brightness temperature. The solid line shows the spectrum for a 10^6 K corona and 10^4 K chromosphere. The dashed line shows the spectrum for the coronal contribution alone.

ture and density than assuming a single-temperature corona. The fact that the optically thick part of the spectrum gives directly the electron temperature as a function of frequency, and hence height, can be used to determine the LOS variation. In fact, Grebinskij *et al.* (2000; see also Chapter 6) show that precise measurement of the spectral slope and the degree of polarization are sufficient to determine the longitudinal component of B. Figure 4.3 demonstrates that this simple technique works amazingly well, at least for model data. The relatively low degree of polarization, and the need for smooth and accurate brightness temperature spectra, make this a challenging but rewarding observational application for FASR.

5. Gyroresonance Diagnostics

The free-free emission diagnostics can be used everywhere in the solar atmosphere that the magnetic field is not too strong ($B \leq 100$ G). However, in
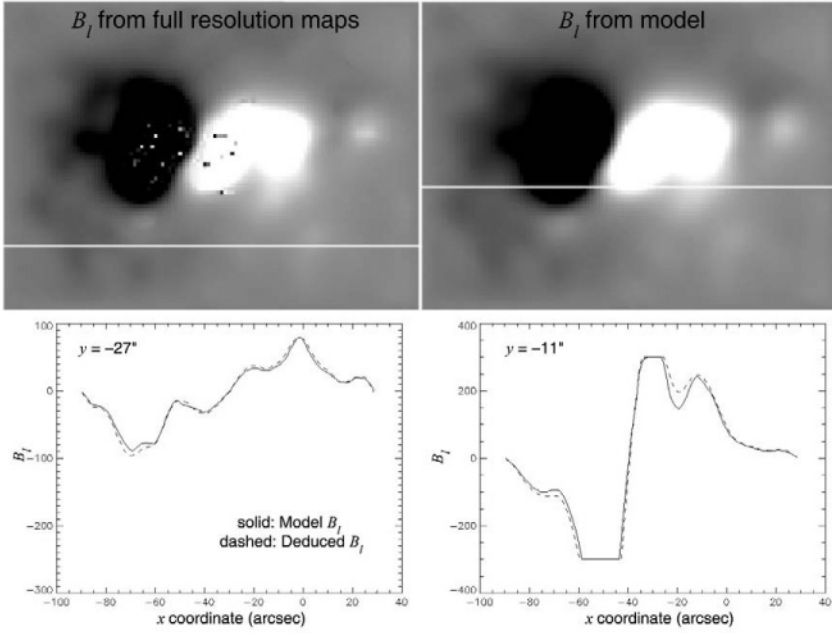
Figure 4.3. Longitudinal magnetic field from the model atmosphere given by Mok *et al.* (2003), compared with the field deduced from radio spectra from the model. The model is shown on the upper right, and the deduced longitudinal magnetogram is shown on the upper left. The salt and pepper in the deduced field map is due to failure of the algorithm in regions of high field strength, where gyroresonance emission strongly affects the spectrum. The horizontal white lines indicate the locations of the 1-dimensional profiles shown in the lower panels, for quantitative comparison. The excellent quantitative comparison (see Gary 2003) shows that the method, from Grebinskij *et al.* (2000) works very well.

the lower corona above active regions a different mechanism, gyroresonance emission, dominates as detailed in Chapter 5. The expression for gyroresonance opacity from thermal electrons, is given by Dulk (1985) as

$$\kappa_\nu(s,\theta) = \frac{\pi^2}{4c} \frac{1}{\mu_\sigma \partial(\omega\mu_\sigma)/\partial\omega} \frac{\nu_p^2}{\nu} \frac{s^2}{s!} \left(\frac{s^2\beta^2\sin^2\theta}{2}\right)^{s-1} \frac{1}{\beta|\cos\theta|} \tag{4.8}$$

$$\times \exp\left[-\frac{(1-s\nu_B/\nu)^2}{(2\mu_\sigma^2\beta^2\cos^2\theta)}\right](1-\sigma|\cos\theta|)^2 \tag{4.9}$$

where μ_σ is the refractive index for magneto-ionic mode σ ($\sigma = +1$ for *o*-mode and -1 for *x*-mode), $\beta = k_B T/m_e c^2$, θ is the direction of the magnetic field to the line of sight, and the other parameters are as defined earlier. Spectra from

gyroresonance sources, again assuming an isothermal corona, are characterized by a flat optically thick portion at low frequencies, becoming optically thin and falling steeply at high frequencies. The frequency at which the steep decline occurs is $\nu = s\nu_B$, where s is the highest optically thick harmonic, typically $s = 3$ for x-mode and $s = 2$ for o-mode, and ν_B is the gyrofrequency for the highest magnetic field strength along the line of sight that remains at coronal temperatures, as discussed by White in Chapter 5. Note that gyroresonance measures the total magnetic field, as distinct from longitudinal component of magnetic flux, discussed in the previous section.

Neglecting variations of T_e along the line of sight, the spectral shape for thermal gyroresonance emission is again invariant. The Universal Spectrum for this mechanism is as shown in Figure 4.4, where the arrows again indicate the shift in the position of the spectrum for factor of 4 changes in T_e and B. Note that the electron density and the angle, θ, that B makes to the line of sight also affect the shape, but in a discrete way by changing which harmonic is optically thick. The spectrum shown by the dashed line illustrates a typical change in shape when density or angle θ (both assumed constant along the line of sight) drops enough that the $s = 3$ layer becomes only partially optically thick, but $s = 2$ remains optically thick. In this case, the spectrum falls steeply at frequency $\nu = 2\nu_B$, to the brightness temperature $T_b = T_{\text{cor}}\tau$, where $\tau < 1$ is the optical depth at the $s = 3$ layer. The arrow on the horizontal branch of the dashed spectrum shows the shift expected for an increase in $n_e(\sin\theta)^{2s-2}$ by a factor of 4. Because the optical depth of o-mode emission is less than that of x-mode, both spectral shapes in Figure 4.4 can occur along the same line of sight, with the solid line representing the x-mode, and the dashed line representing the o-mode. More complicated spectra are possible in which both x-mode and o-mode spectra may display harmonic changes. In any case, key diagnostic information can be gleaned from measuring spectra in both circular polarizations, which essentially give two independent, but mutually consistent diagnostics of plasma parameters along the line of sight. Such spectral features have been observed with OVSA when the spatial geometry could be accounted for, either by modeling (Hurford & Gary 1986) or by direct imaging (Gary & Hurford 1994—see Chapter 2, Fig. 2.2).

FASR will produce the first brightness temperature spectra of sufficient spatial and spectral resolution that the spectral discontinuities of the type shown by the dashed line in Figure 4.4 will be well resolved on a routine basis. The spectra in Figure 4.5 are derived from an active region model by Mok *et al.* (2004). The model parameters of B, n_e, and T were used to calculate radio emission maps at 100 frequencies, and the figure shows the resulting spectra at two points in the active region, in both right and left circular polarization, after folding through the expected FASR instrumental response. Such spectra will be available at every resolution element in the maps. This demonstrates that
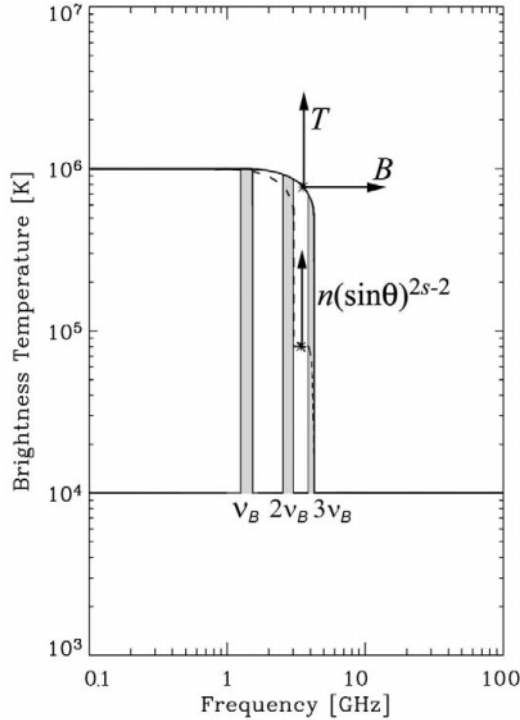
Figure 4.4. "Universal Spectra" for gyroresonance emission. See text for details.

parameters of electron temperature and magnetic field strength can be simply determined directly from such spectra. Thus, FASR will provide precise diagnostics without the need for assumptions of constant T_e, n_e, or $\sin\theta$ along the line of sight.

In the more general case, the optically thick spectral shape will be a sensitive measure of the variations of T_e as a function of B, while the spectral shapes of optically thin "plateaus" will indicate changes in n_e and θ with B. In practice, the dependence on θ is rather steep and will likely swamp the linear dependence on n_e. Time variations in the shape of these plateaus will provide a sensitive measure of large-scale oscillations in the direction of the magnetic field, as has already been shown with single- and dual-frquency observations (Shibasaki 2001; Nindos *et al.* 2002). The conversion of variations of T_e as a function of B to T_e as a function of absolute distance along the line of sight, of course, requires a knowledge of the dependence of B along the line of sight, which is an unsolved problem. Careful analysis based on photospheric field extrapolations, indications from observations at other wavelengths, and physical relationships
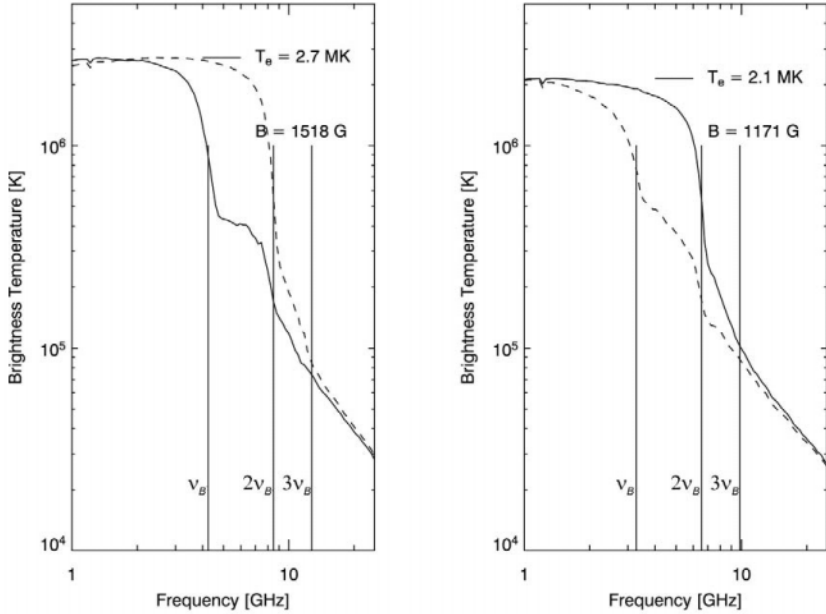
Figure 4.5. The right-hand circular polarization (RCP, solid curve) and left-hand circular polarization (LCP, dashed curve) radio emission spectra at two lines of sight in a model active region, as calculated at 100 frequencies from 1–24 GHz, after folding through the instrumental response. The electron temperature of the corona can be read directly from the spectra at low frequencies, where the emission is optically thick. The frequency at which abrupt drops in brightness occur are identified with different harmonics of the gyrofrequency (vertical lines), allowing the magnetic field strength to be unambiguously determined.

such as pressure balance and continuity offer the prospect that a full 3-D model of the solar active region atmosphere could be obtained. This lofty goal has not been accomplished to date, but efforts are underway (e.g. Mok *et al.* 2001; 2004).

6.   Gyrosynchrotron Diagnostics

The main emission mechanism during solar flares, at least at frequencies > 3 GHz, is gyrosynchrotron emission from mildly-relativistic electrons of order several hundred keV. For such energies, the theoretical expressions must be solved numerically. The spectral shapes expected from thermal and powerlaw nonthermal isotropic electron distributions were given by Dulk (1985), along with empirical powerlaw expressions for emissivity, opacity, effective temperature, degree of polarization, and others, obtained from fits to the numerical

results. For powerlaw electron distributions, the spectral shapes remain invariant with such parameters as number density of fast electrons, magnetic field strength and direction, but the slopes of the spectrum do vary with electron powerlaw index δ. The concept of Universal Spectra can still be used for homogeneous sources in this case, so long as the variation in spectral slope with δ is specified.

Figure 4.6 shows the resulting Universal Spectra, again for homogeneous sources, for both thermal and powerlaw nonthermal distributions (left and right panels respectively). The arrows indicate the direction and magnitude of shift for increases in the labeled parameter by a factor of 4. The positive slope on the optically thick (low frequency) side of the brightness temperature spectrum is due to the rising effective energy, E, of the electrons producing the emission, $T_b = E/k_B$. Changes in the column density, $N_e L$ shift the spectra nearly parallel to this rising slope. The optically thin (high frequency) slope is directly proportional to the powerlaw index of the electron energy distribution. The spectra in each panel shown by the dashed lines schematically indicate the o-mode emission, to show the typical spectral pattern of circular polarization expected from a homogeneous source.

However, several effects can alter these simple relationships, even for a homogeneous source. On the optically thick side, the ambient medium can affect the shape either because of extra absorption by co-spatial thermal plasma (e.g. Benka & Holman (1992), or by suppression of the emission due to Razin Suppression (at frequencies $\nu < 20 n_e / B$). On the optically thin side, recent work by Fleishman & Melnikov (2003ab) shows that non-isotropic pitch angle distributions for the electrons can significantly alter the high-frequency slope, and greatly change the polarization. Observationally, flaring loops have been imaged typically at two frequencies (e.g. Dulk *et al.* 1986; Nindos *et al.* 2000; Melnikov *et al.* 2002), although some events have been imaged at many frequencies (e.g. Lim *et al.* 1994; Wang *et al.* 1994; 1995; 1996) with moderate spatial resolution. Observations of the spectral and spatial dynamics of flaring loops (Lee *et al.* 2000; Lee & Gary 2001; Melnikov *et al.* 2002) are particularly useful as diagnostics of the evolution of accelerated electrons (see Chapter 9).

FASR will give spatially resolved spectra with sufficient quality and spatial resolution to measure the detailed changes in the spectrum at different points along flaring loops. The peak frequency of such spectra alone is enough to constrain the relative magnetic field strength along the loop, as shown in Figure 4.7. The optically thin slope directly yields the energy distribution of electrons, and possible changes with position in the loop due to transport effects, collisions, and wave-particle interactions.
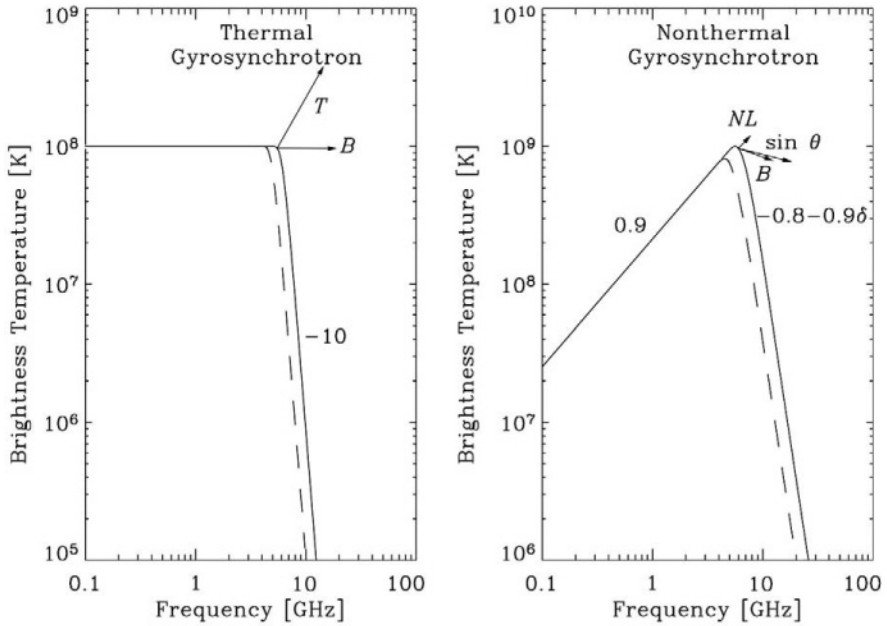
Figure 4.6. "Universal Spectra" for gyrosynchrotron emission, for a homogeneous source with thermal (left panel) or powerlaw (right panel) electron energy distributions. The solid lines show the x-mode spectra, while the dashed lines schematically show the o-mode spectra. Thermal spectra are distinguished by their flat optically thick slope, and very steep optically thin slope.

7. Exotic Mechanisms

In addition to these standard mechanisms, others have been proposed to explain certain kinds of observed emission. Here we briefly mention the Electron Cyclotron Maser (ECM) mechanism and Transition Radiation.

ECM (Holman *et al.* 1980; Melrose & Dulk 1982) is expected to operate in convergent magnetic fields in the legs of loops, where downward moving electrons escape the magnetic trap. The remaining particles form an anisotropic pitch angle distribution, which is unstable to ECM emission. The coherent emission occurs in clusters of short duration ($\sim$ 10 ms), narrowband ($\sim$ 10 MHz), high brightness ($\sim 10^{12}$ K) bursts called spike bursts. Too little is known about the spatial and spectral characteristics of ECM emission to develop spectral diagnostics (in fact, there is uncertainty whether spike bursts are due to ECM or other wave instabilities—see Chapter 10), and it may be that any such diagnostics would relate only to the detailed microphysics in the source region. Accounting for the generation and escape of the radiation may yield constraints on the surrounding plasma, however.
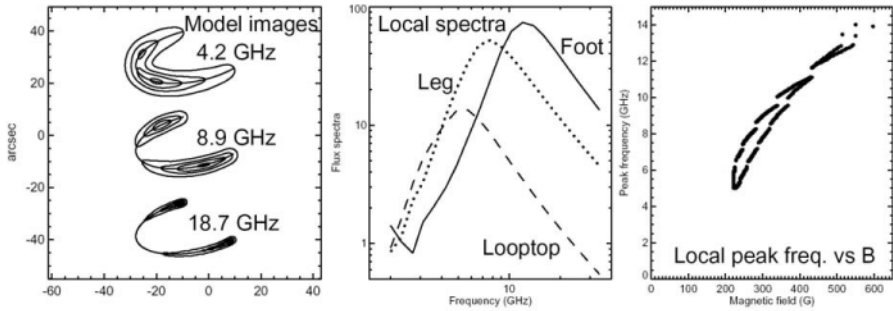
Figure 4.7. Gyrosynchrotron emission from a model coronal magnetic loop. The panel at left shows how the appearance of the loop changes from low optically thick frequencies (4.2 GHz) where the loop dominates to high optically thin frequencies (18.7 GHz) where the footpoints dominate. The thin solid line inicates the spine of the loop in each case. In the middle panel are plotted local radio spectra at three different locations within the loop: at a footpoint (solid line), at the top of the loop (dashed line), and at a location half-way up the leg of the loop (dotted line). In the right panel we plot the frequency of the peak of the radio spectrum versus the local magnetic field, showing that there is a nearly linear dependence of the spectral peak on the local magnetic field and thus spatially-resolved spectroscopy can be used to measure the variation of magnetic field along the loop. Figure by S. White, private communication.

Transition Radiation (TR) arises not due to the usual electron accelerations, but rather due to electrons moving with constant velocity through a medium with inhomogeneities or discontinuities in the dielectric constant of the medium. Although the TR theory is quite old, a full understanding of the observational characteristics had to await more recent developments in the theory (Platonov & Fleishman 1994; Platonov & Fleishman 2002). The intensity of transition radiation had been predicted to be very small and perhaps unobservable, until Platonov & Fleishman (1994) discovered that the intensity is greatly enhanced at frequencies just above the local plasma frequency. The radiation in this form is referred to as resonant transition radiation (RTR), since the plasma response to the external excitation is strengthened around the resonant frequency of the medium (Platonov & Fleishman 1994; Platonov & Fleishman 2002). The RTR emission is observable for any source when a sufficient level of small-scale inhomogeneity is present, and the emission is observed at frequencies covering the characteristic plasma frequency of the source. These conditions are met in the decimetric frequency range in the solar corona. Thus, fast electrons accelerated in solar flares can be expected to produce observable RTR in certain conditions. The problem is to recognize it in the presence of simultaneously occurring competing mechanisms, such as gyrosynchrotron emission, electron-

cyclotron emission, or coherent plasma emission. The theory of transition radiation generated by fast particles is discussed in detail in a recent review paper by Platonov & Fleishman (2002).

8.   Conclusion

This chapter has reviewed mechanisms relevant to solar radio emission with emphasis on the resulting spatially-resolved spectra. The regimes of applicability of these different mechanisms are explained in terms of the relative values of the local plasma frequency, gyrofrequency and the frequency at which free-free emission becomes optically thick. In the case of incoherent emission (free-free, gyroresonance, thermal and nonthermal gyrosynchrotron), so-called "Universal Spectra" show that *for uniform source parameters along a line of sight*, the spectral shapes are invariant, with spectral parameters readily related to the electron and magnetic field parameters. Changes in these physical parameters from point to point in the solar atmosphere merely act to shift the location of the Universal Spectra while maintaining their shape. For non-uniform parameters along the line of sight, the shapes can change due to superposition of contributions of the invariant spectra for a given mechanism, or even contributions from multiple mechanisms. However, we also outline basic approaches whereby such contributions can be inverted, given the high quality spectra expected from FASR, so that 3-dimensional solar radio diagnostics can be anticipated. A key reason that this can be done for radio emission, in contrast to the case of X-ray or EUV emission, is that the radio emission is optically thick at some frequencies and optically thin at others. Thus, the "line of sight" is really many lines of sight of different lengths at different frequencies, giving extra information about the distribution of plasma parameters along the line of sight. As we mentioned earlier, additional information can be gleaned from measuring spectra in both circular polarizations, which essentially give two independent, but mutually consistent diagnostics of plasma parameters along the line of sight.

The "Universal Spectra" approach that we have outlined is thus meant to be schematic only, to demonstrate the basics of using the radio spectrum to deduce both parameters of the solar atmosphere and characteristics of energetic particles in flaring regions. The high spatial and spectral resolution FASR data will permit far more sophisticated analysis, yielding a diagnostic precision far greater than any so far available. In fact, the anticipation of FASR observations is already spurring theoretical and modeling efforts to explore the range of new diagnostics that FASR will make possible, some of which are described in this book. Even more exciting, the FASR data will undoubtedly show many puzzling features that will not agree with our naive models, and so will lead to new understanding of the solar atmosphere and flaring loops.

Acknowledgments

References

Bastian, T. S., Ewell, M. W., & Zirin, H. 1993, ApJ, 415, 364

Benka, S. G. & Holman, G. D. 1992, ApJ, 391, 854

Boischot, A. 1959, Ann. Astrophys. 21, 273

Dulk, G. A. & McLean, D. J. 1978, Solar Phys, 57, 279

Dulk, G. A. 1985, ARAA, 23, 169

Dulk, G. A., Bastian, T. S., & Kane, S. R. 1986, ApJ, 300, 438

Fleishman, G. D. & Melnikov, V. F. 2003a, ApJ, 584, 1071

Fleishman, G. D. & Melnikov, V. F. 2003b, ApJ, 587, 823

Gary, D. E. & Hurford, G. J. 1994, ApJ, 420, 903

Grebinskij, A., Bogod, V., Gelfreikh, G., Urpo, S., Pohjolainen, S., & Shibasaki, K. 2000, A&AS, 144, 169

Holman, G. D., Eichler, D., & Kundu, M. R. 1980, IAU Symp. 86: Radio Physics of the Sun, 86, 457

Hurford, G. J. & Gary, D. E. 1986, Coronal and Prominence Plasmas, 319

Hurford, G. J., Gary, D. E., & Garrett, H. B. 1985, Radio Stars; Proceedings of the Workshop on Stellar Continuum Radio Astronomy, 379

Lee, J. & Gary, D. E. 2000, ApJ, 543, 457

Lee, J., Gary, D. E., & Shibasaki, K. 2000, ApJ, 531, 1109

Lim, J., Gary, D. E., Hurford, G. J., & Lemen, J. R. 1994, ApJ, 430, 425

Melnikov, V. F., Reznikova, V. E., Yokoyama, T., & Shibasaki, K. 2002, The 10th European Solar Physics Meeting, (Ed. A. Wilson.), ESA SP-506, Vol. 1. 339

Melrose, D. B. & Dulk, G. A. 1982, ApJ, 259, 844

Mok, Y., Lionello, R., Mikic, Z., & Linker, J. 2004, ApJ, submitted

Mok, Y., Lionello, R., Mikic, Z., & Linker, J. 2002, American Astronomical Society Meeting, 200, abstract #2.12

Mok, Y., Lionello, R., Mikic, Z., & Linker, J. 2001, American Geophysical Union, Spring Meeting 2001, abstract #SH41A-20, 41

Nindos, A., White, S. M., Kundu, M. R., & Gary, D. E. 2000, ApJ, 533, 1053

Nindos, A., Alissandrakis, C. E., Gelfreikh, G. B., Bogod, V. M., & Gontikakis, C. 2002, A&A, 386, 658

Platonov, K. Y. & Fleishman, G. D. 1994, Journal of Experimental and Theoretical Physics, 79, 572

Platonov, K. Y. & Fleishman, G. D. 2002, Uspekhi Fizicheskikh Nauk, 45, 235

Saito, K., Makita, M., Nishi, K., & Hata, S. 1970, Annals of the Tokyo Astronomical Observatory, 12, 51

Shibasaki, K. 2001, ApJ, 550, 1113

Vernazza, J. E., Avrett, E. H., & Loeser, R. 1981, ApJ Supp., 45, 635

Wang, H., Gary, D. E., Zirin, H., Nitta, N., Schwartz, R. A., & Kosugi, T. 1996, ApJ, 456, 403

Wang, H., Gary, D. E., Zirin, H., Kosugi, T., Schwartz, R. A., & Linford, G. 1995, ApJ, 444, L115

Wang, H., Gary, D. E., Lim, J., & Schwartz, R. A. 1994, ApJ, 433, 379

Wild, J. P. & McCready, L. L. 1950, Aust. J. Sci. Res., A-3, 387

Wild, J. P., Sheridan, K. V., & Trent, G. H. 1959, in Paris Symp. on Solar Radio Astronomy, Ed. R.N. Bracewell, Stanford Univ. Press, 176